Supplementary Materials

Direct Z-scheme siloxene germanane nanosheet heterojunctions for broadband photodetection and ultrasensitive photoelectrochemical sensing

Runqi Liu[1,2,3,#], Huiyu Chen[1,2,3,#], Weikang Yuan[1,2,3], Hui Fu[1,2,3], Fulai Zhao[1,2,3,4], Yiyu Feng[1,2,3]

[1]Discipline and Technology Center for High Temperature Functional Ceramics, Shandong University of Technology, Zibo 255000, Shandong, China.
[2]Shandong Key Laboratory of Functional-Structural Integrated Ceramics, Shandong University of Technology, Zibo 255000, Shandong, China.
[3]School of Materials Science and Engineering, Shandong University of Technology, Zibo 255000, Shandong, China.
[4]Shandong Chambroad Holding Group Co., Ltd., Binzhou 256500, Shandong, China.
[#] Authors contributed equally.

Correspondence to: Prof. Fulai Zhao, Discipline and Technology Center for High Temperature Functional Ceramics, Shandong University of Technology, Zibo 255000, Shandong, China; Shandong Key Laboratory of Functional-Structural Integrated Ceramics, Shandong University of Technology, Zibo 255000, Shandong, China; School of Materials Science and Engineering, Shandong University of Technology, Zibo 255000, Shandong, China; Shandong Chambroad Holding Group Co., Ltd., Binzhou 256500, Shandong, China. E-mail: jayfly@sdut.edu.cn

Table of Contents

Materials and apparatus

Germanium (Ge powder, 99.999%, Macklin), calcium (Ca, 99.5%, aladdin), calcium silicide ($CaSi_2$, tech. Ca≈30%, may contain up to 5% Fe, Alfa Aesar Chemicals), sodium hydroxide (NaOH, 97%, Energy Chemical), concentrated hydrochloric acid (HCl, AR, 37%), ultra-pure water (H_2O, HPLC, Concord technology), Isopropyl alcohol (C_3H_8O, AR, HPLC, Energy Chemical), Barium sulfate ($BaSO_4$, SP, Rhawn), ethanol (EtOH, 99.5%, SuperDry, J&KSeal, J&K Scientific), polyvinyl pyrrolidone (PVP, M_w = 1300000, Heowns). All chemical reagents were used without further purification, but $CaSi_2$ was washed with concentrated NaOH solution (2M) to remove impurities before use.

X-ray diffraction (XRD) was performed on a D8 Advanced X-ray diffractometer (BRUKER AXS GMBH) under Cu Kα radiation at a wavelength of 0.154 nm. Fourier transform infrared (FTIR) spectroscopy was carried out on an FTIR 650 spectrometer (BRUKER AXS GMBH) with KBr discs. Raman spectra were acquired with a DXR Raman microscope from Thermo Scientific using a 532 nm laser source. Solid-state ultraviolet-visible-near-infrared (UV-Vis-NIR) spectroscopy were recorded with a Lambda 750 UV/Vis/NIR spectrophotometer (Perkin Elmer) by mixing samples thoroughly with $BaSO_4$ powder and spreading them evenly on a $BaSO_4$ background holder. The Kubelka-Munk remission function was employed to convert the measured reflectance to absorption. X-ray photoelectron spectroscopy (XPS) measurements were performed at a power of 450 W using a PHI 1600 surface analysis system equipped with a Mg Kα anode. Field-emission scanning electron microscopy (FESEM) images were recorded by a Hitachi S-4800 field-emission scanning electron microscope equipped with an energy-dispersive X-ray spectrometer (EDS). Transmission electron microscopy (TEM) images, selected area electron diffraction (SAED) patterns, high-angle annular bright-field scanning TEM (STEM) images, and EDS images were collected with a JEOL JEM-2100F field-emission Electron Microscope equipped with an electric-cooling energy-dispersive X-ray spectrometer (EDS) and scanning tunneling microscope (STM) probe. Fluorescence spectra (FL) were recorded with a Hitachi F-4600 fluorescence spectrophotometer at room temperature. A Dimension ICON-PT (BRUKER AXS GMBH) atomic force microscope (AFM) was employed to investigate the morphology and thickness of samples.

Synthesis of germanane and siloxene

Germanane and siloxene were synthesized according to the literature[1, 2]. Firstly, the $CaGe_2$ precursor was synthesized by annealing stoichiometric ratios of Ca and Ge in a vacuum sealed quartz tube at 1050 °C for 20 h. Then $CaGe_2$ crystals were stirred in concentrated HCl for 8 days at −30 °C. Germanane was obtained by washing the resulting products with ultra-pure water and isopropyl alcohol. Siloxene was synthesized through a topochemical reaction of $CaSi_2$ with concentrated HCl at 0 °C under argon atmosphere, followed by washing with ultra-pure water and isopropyl alcohol. Both the germanane and siloxene products were vacuum dried at 60 °C to obtain a dried powder.

Preparation of few-layer germanane and siloxene nanosheets

To prepare germanane/siloxene heterostructures, few-layer GeNSs and SiNSs were obtained by the PVP solution-assisted ultrasonic exfoliation. Germanane or siloxene with PVP in a mass ratio of 5:1 was dissolved in ultra-dry ethanol under argon atmosphere, the solution was then sealed and ultrasonicated at 3 ℃ in a KQ-50TDE benchtop ultrasonic bath at a power of 90% for 6 h. Then the dispersion was centrifuged with a TG16-WS centrifuge at 3000 rpm for 30 min to obtain the supernatant of few-layer nanosheets. The obtained supernatant was then centrifuged at 11000 rpm to obtain a precipitate, which was then dried at 60 °C for 24 hours to prepare GeNSs and SiNSs powders.

Preparation of layered 2D/2D GeNSs/SiNSs nanocomposites

GeNSs and SiNSs powders were weighed according to the mass ratio of 1: 9, 3: 7, and 1: 1, respectively. Then GeNSs and SiNSs powders were ultrasonically dispersed in EtOH at a concentration of 10 mg/mL, respectively, to form uniform solutions. Then each pair of GeNSs solution and SiNSs solution were mixed together, respectively. Subsequently, the three mixed solutions were ultrasonicated for 10 min to form homogeneous solutions. The mixed solutions were vacuum filtered, and dried under vacuum at room temperature for 24 h to obtain GeNSs/SiNSs nanocomposites, which were named as H1, H2 and H3, respectively.

Photoelectrochemical measurement

Photoelectrochemical measurements were performed at room temperature on an electrochemical workstation (CHI 660d) with a three-electrode cell (using a 0.5 M Na_2SO_4 electrolyte). The working electrodes were prepared by dropping the sample slurry (30 mg dispersed in 2 mL EtOH with 200 μL0.5 wt% Nafion) on an ITO substrate (coating area1.0 cm^2) and then drying in air at 60 °C. A Pt plate was used as the counter electrode, and a saturated calomel electrode (SCE) was used as the reference electrode for transient photocurrent responses (I–t curves) test and Mott Schottky test. Electrochemical impedance spectroscopy (EIS) measurements were performed in the frequency range from 100 mHz to 1 MHz with an AC voltage of 5 mV. Amperometric i-t curves were recorded under the conditions of bias potential of 0, 0.3, and 0.6 V and an interval of 5 s. Various lights including 300 W xenon lamp irradiation, and monochromatic light of 365, 405, 520, 635, 750, 808, and 980 nm were used to irradiate the working electrode, and the light power intensities were labeled as level I, II, III, IV (Table S1).

Table S1. The light power density (P_λ) of the incident light with various irradiation wavelengths. The gradually increased P_λ were labelled with I, II, III, and IV levels, respectively

P_λ (mW·cm^{-2})	I	II	III	IV
365 nm	40.5	83.8	115.0	150.6
405 nm	45.3	85.4	118.6	150.4
520 nm	42.4	81.8	118.1	133.8
635 nm	44.0	81.6	118.0	150.9
750 nm	41.7	83.8	110.9	152.4
808 nm	43.8	82.9	112.0	153.6
980 nm	43.2	81.8	118.8	151.6

Theoretical calculations

All calculations were performed using the Vienna *ab initio* simulation package (VASP) under the density-functional theory (DFT) framework[3, 4]. The generalized gradient approximation with the Perdew-Burke-Ernzerhof functional (GGA-PBE)[5]was used for the electron exchange and correlation. In order to capture the vdW interactions, the correction method of Grimme's DFT-D2 was especially considered for the germanane-siloxene heterojunction[6]. Additionally, projected augmented wave (PAW) potentials were used to describe the ionic cores, and valence electrons were taken into account using a plane wave basis set with a kinetic energy cutoff of 600 eV[7, 8]. The valence electron configurations applied in this work are $3d^{10}4s^24p^2$ (Ge), $3s^23p^2$ (Si), $2s^22p^4$ (O) and $1s^1$ (H). All structures were considered non-magnetic. A 13×13×1 Monkhorst-Pack ***k***-point grid was used for the Brillouin zone sampling for all structures. A vacuum layer of 20 Å was chosen to avoid the interactions of the adjacent cells along the *z*-direction. The stacking pattern of the heterojunction is shown below. The lattice parameter of the heterojunction is the same as the fully relaxed germanane.

The partial occupancies of the Kohn−Sham orbitals were allowed using the Gaussian smearing scheme with a smearing width of 0.03 eV for structural optimization, and the tetrahedron method with Blöchl corrections was used for accurate energy and density of states calculations[9, 10]. The electronic energy was considered convergent when the energy change is smaller than 10^{-5} eV per simulation cell. The structures were fully relaxed until the residual forces are less than 10^{-2} eV/Å.

The binding energy between single-layer germanane and single-layer siloxene is calculated by Equation (1).

$$E_b = E(Ge_2Si_2OH_4) - E(Si_2OH_2) - E(Ge_2H_2) \quad (1)$$

Where the unit of binding energy E_b is f.u., Ge_2H_2 represents single-layer germanane, Si_2OH_2 represents single-layer siloxene, and $Ge_2Si_2OH_4$ represents germanane-siloxene heterojunction.

Frequency dependent dielectric functions were calculated using the independent-particle approximation implemented in VASP[3, 4]. The optical absorption coefficients were calculated by Equation (2).

$$\alpha(\omega) = \sqrt{2\omega}\left[\sqrt{\varepsilon_1^2(\omega) + \varepsilon_2^2(\omega)} - \varepsilon_1(\omega)\right]^{\frac{1}{2}} \quad (2)$$

Characterization of GeNSs/SiNSs nanocomposites

The characterization results of the chemical and crystal structures of the as-prepared nanocomposites are shown in Figure S1C-E. The FTIR spectra in Figure S1C indicates that GeNSs/SiNSs nanocomposites exhibit the clear main characteristic peaks of pure pure germanane and siloxene. The broad peaks in the range of 3000 to 3600 cm^{-1} are ascribed to the stretching vibration of O-H of H_2O. The peaks at 2002 and 478 cm^{-1} could be identified as the Ge–H stretching and Ge–H wagging modes of germanane, respectively. In siloxene, a series of peaks at 417, 636, 880, 1072, 1640, and 2108 cm^{-1}, are consistent with the v(Si–Si), δ(Si–H), v(Si–OH), v(Si–O), v(Si–H), and v((Si3)≡Si–H), respectively. Raman spectra (Figure S1D) of siloxene show peaks at 328, 374, and 490 cm^{-1}, which are corresponded to the Si-Si bonds, peaks at 633 and 728 cm^{-1} are assigned to Si-H bonds, the one at 2114 cm^{-1} is ascribed to the Si-H_2 bond[11, 12]. The peak at 290 cm^{-1} in germanane is attributed to the phonon modes of Ge-Ge bonds. All Raman characteristic peaks of both germanane and siloxene can be observed in GeNSs/SiNSs composite samples. In situ XPS measurements were performed using a Thermofisher ESCALAB 250Xi surface analysis system equipped with an Al Kα anode. A 300 W Xe lamp was used as a light source. Electron paramagnetic resonance (EPR) spectra were collected using a BRUKER A300 EPR spectrometer (77 K, 9.063 GHz, X-band) for the detection •O_2^- and •OH radicals with a 300 W Xe lamp as the light source.

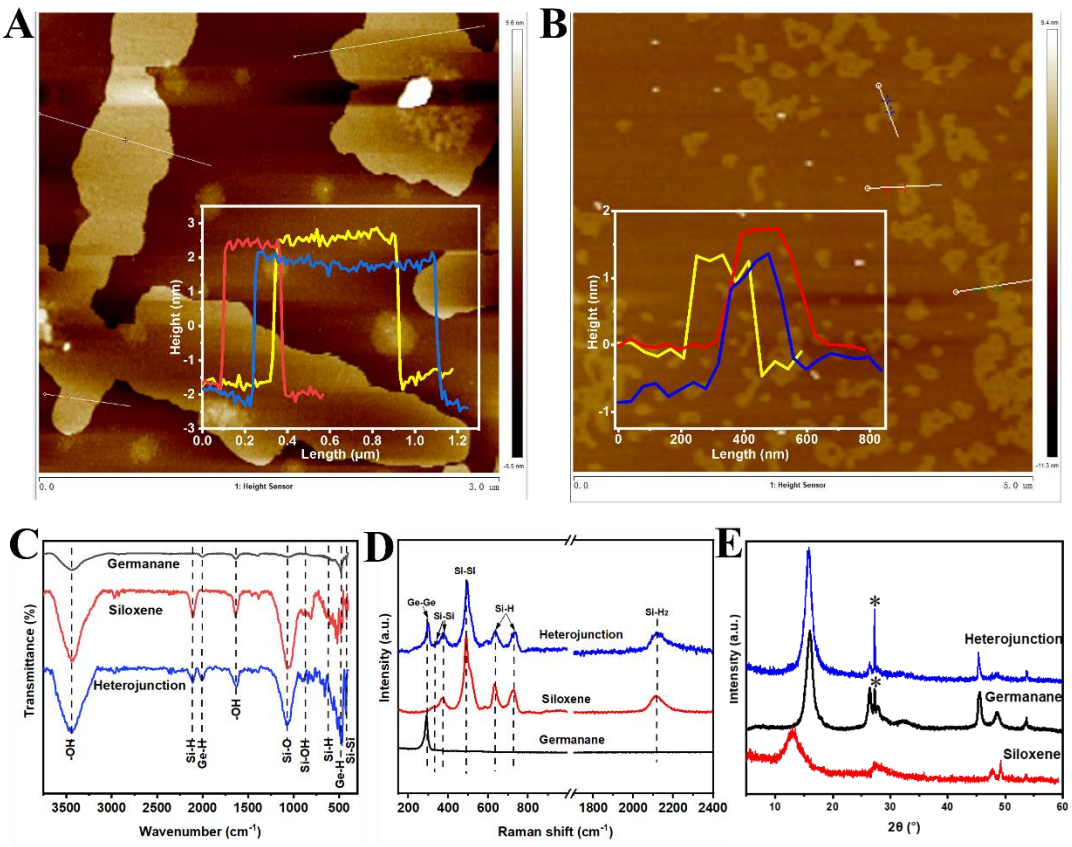

Figure S1. (A-B) AFM images of nanosheets prepared by ultrasonication-centrifugation process. (A) GeNSs, (B) SiNSs. Insets are the corresponding height profiles of nanosheets. (C-E) Chemical structural analysis of germanane, siloxene and GeNSs/SiNSs heterostructure. (C) FTIR spectra, (D) Raman spectra. (E) Crystal structural analysis with XRD spectra for GeNSs, SiNSs and GeNSs/SiNSs heterostructure, where the elemental germanium is marked by an asterisk (*).

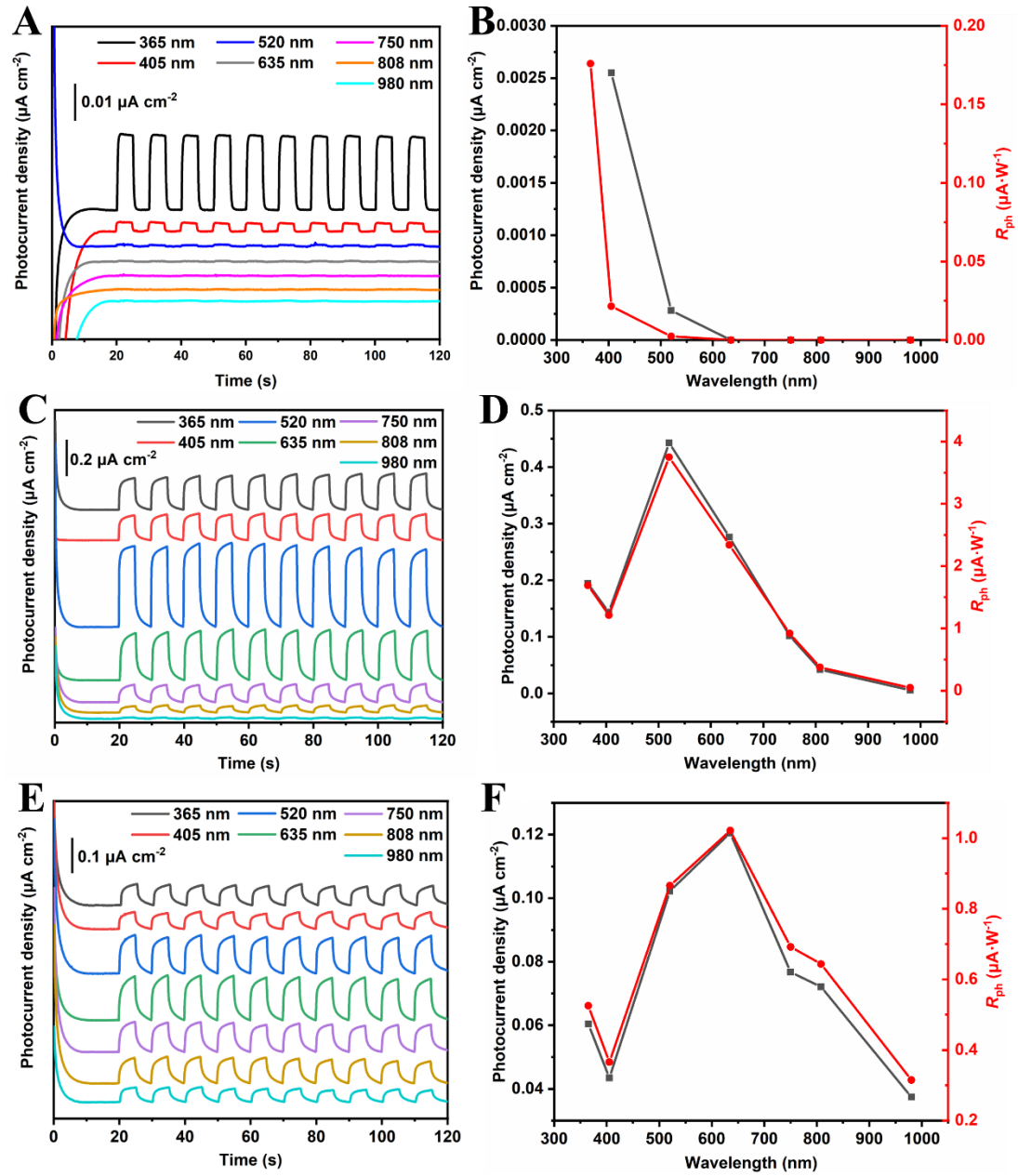

Figure S2. Wavelength-dependent photoresponse of SiNSs (A), H2 (C), and GeNSs (E) and Photocurrent densities and photoresponsivities curves of SiNSs (B), H2 (D), and GeNSs (F) at Level III at 0 V.

The photoresponse performance of PEC photodetectors (PDs) is influenced by the applied bias voltage. Therefore, we tested the photoresponse performance of PDs based on H2 photoelectrodes under different bias voltages. Figure **S3**A shows the optical response performance of H2-PD at a bias voltage of 0, 0.3, and 0.6 V 520 nm at a light power density of 81.8 mW cm^{-2} (Level II). It can be intuitively seen from the figure that with the increase of bias voltage, P_{ph} shows an increasing trend. Under bias voltages of 0, 0.3, and 0.6 V, the P_{ph} of H2-PD is 0.12, 0.74, and 2.04 μA cm^{-2}, respectively, this is because applying a bias voltage on the working electrode can cause potential differences within the material, promoting the separation of photogenerated holes and

electrons, increasing the concentration of photogenerated carriers, and resulting in a significant increase in the P_{ph} of H2-PD with the increase of bias voltage. Therefore, controlling the applied bias voltage can achieve the regulation of H2-PD photoresponse performance. Figure **S3**B is the relationship curve between bias voltage and P_{ph} of H2-PD, which shows the regulatory effect of bias voltage on P_{ph}.

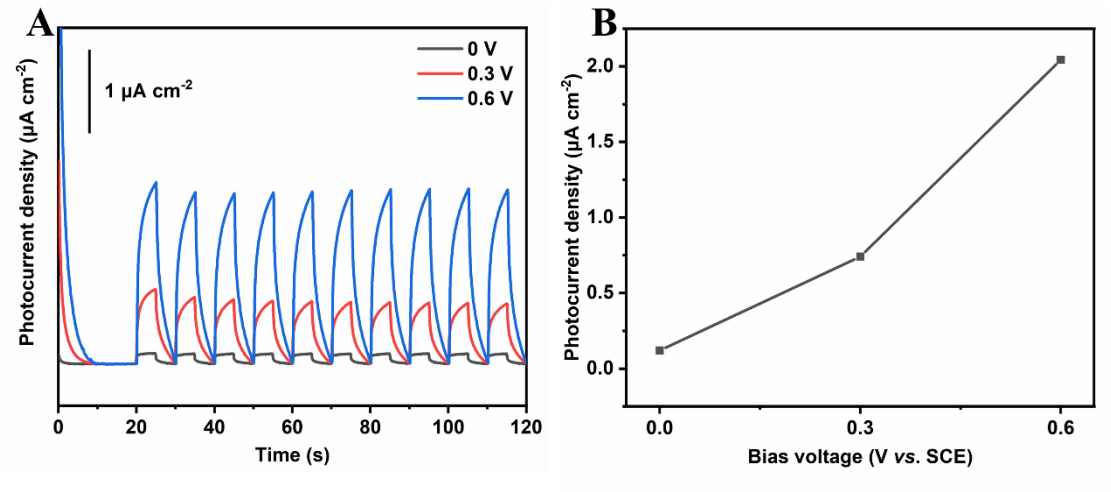

Figure S3. (A) Photoresponse behaviour of H2-photodetector (H2-PD) under bias voltages of 0, 0.3, and 0.6 V illuminated by the light of 520 nm. (B) Photocurrent density of H2-PDs under bias potential from 0-0.6 V.

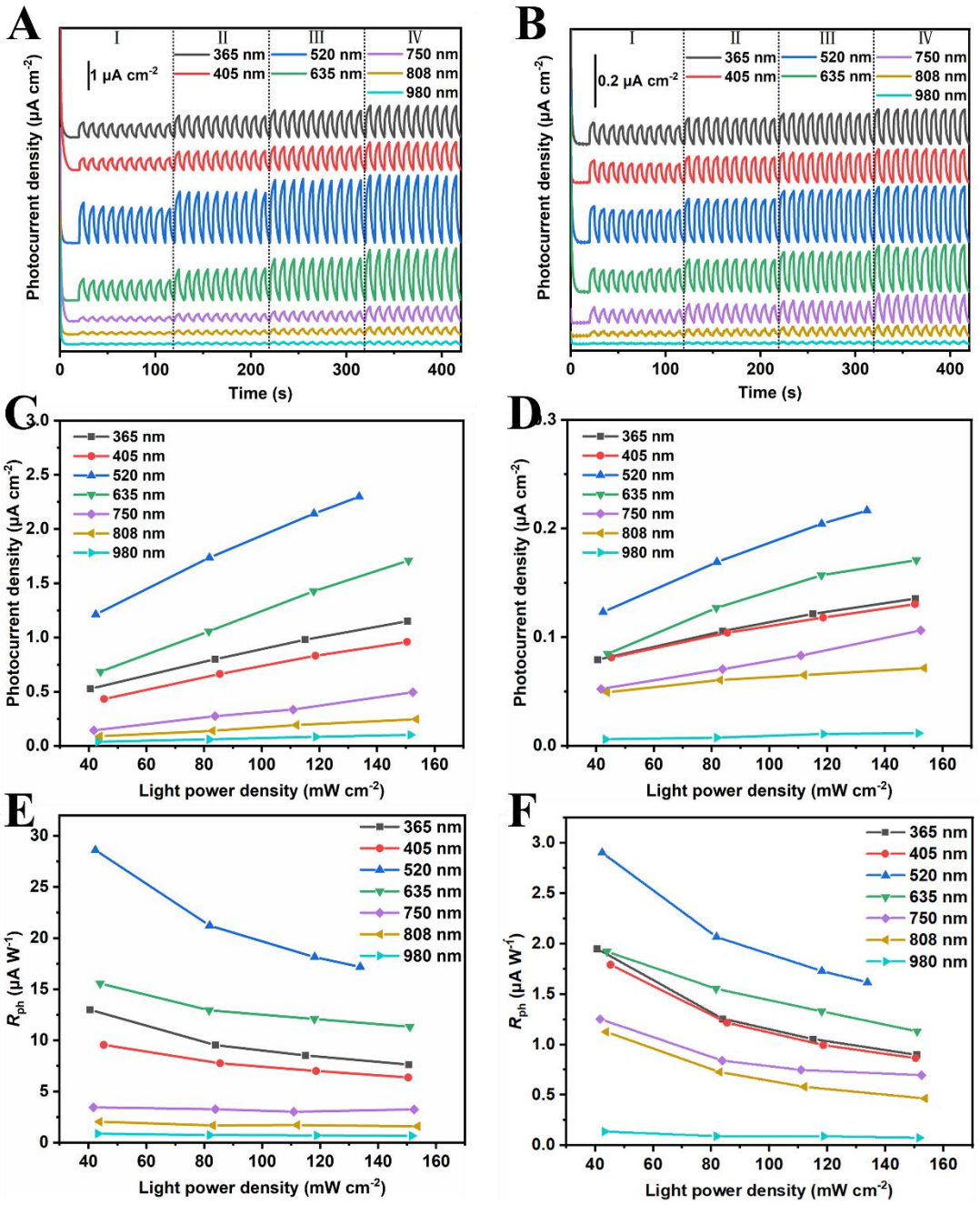

Figure S4. Photoresponse behaviour of H2-PDs illuminated by various wavelengths at 0.6 V (A) and 0 V (B). Curves of P_{ph} as functions of light power intensity P_λ at 0.6 V (C) and 0 V (D). Curves of R_{ph} as functions of light power intensity P_λ at 0.6 V (E) and 0 V (F).

To evaluate the long-term stability of the H2-PD under self-powered conditions (0 V bias), we performed continuous on-off switching tests under 520 nm illumination (Figure S5A). After 3000 s of cycling, the device still exhibited clear on/off switching behavior, and the photocurrent density remained at 75% of its initial value, indicating excellent self-powered cycle stability (Figure S5B). Notably, the photocurrent did not monotonically decay; instead, it showed a slight increase during the first few cycles,

followed by a gradual decline over prolonged operation. This dynamic behavior can be attributed to the interplay between defect-state passivation and interfacial degradation. In the initial stage, shallow trap states at the GeNSs/SiNSs heterojunction interface, such as oxygen vacancies (demonstrated by XPS) and surface dangling bonds, are progressively filled by photogenerated carriers. This trap-filling effect suppresses nonradiative recombination, improving charge separation and transport efficiency, and thus leading to a gradual rise in photocurrent. However, upon extended irradiation, the accumulation of adsorbed electrolyte ions (e.g., SO_4^{2-}) at the electrode surface gradually blocks active sites and increases interfacial charge-transfer resistance. Meanwhile, repeated photoexcitation may also induce mild structural reorganization of the heterojunction. These competing degradation mechanisms eventually dominate, causing the photocurrent to decrease after the initial activation. The overall 75% retention after 3000 s confirms that the long-term stability is primarily limited by surface degradation rather than bulk structural failure.

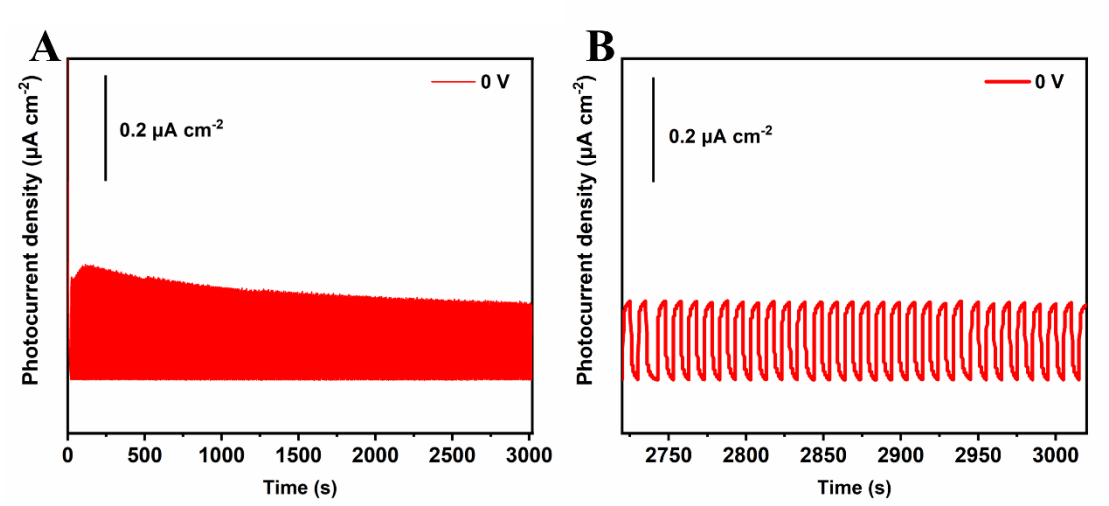

Figure S5. (A) Long-term stability measurement of the H2-photodetector at 0 V under 520 nm with 118 mW cm^{-2} power density, and the enlarged region of (B) 2720−3020 s.

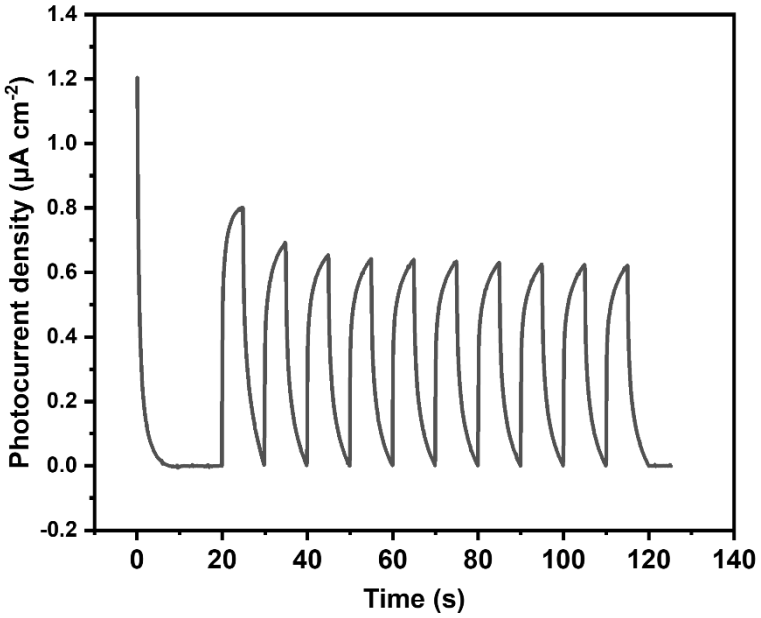

Figure S6. Stability of the H2 electrode-based PEC sensor with tartrazine concentrations of 10^{-11} M.

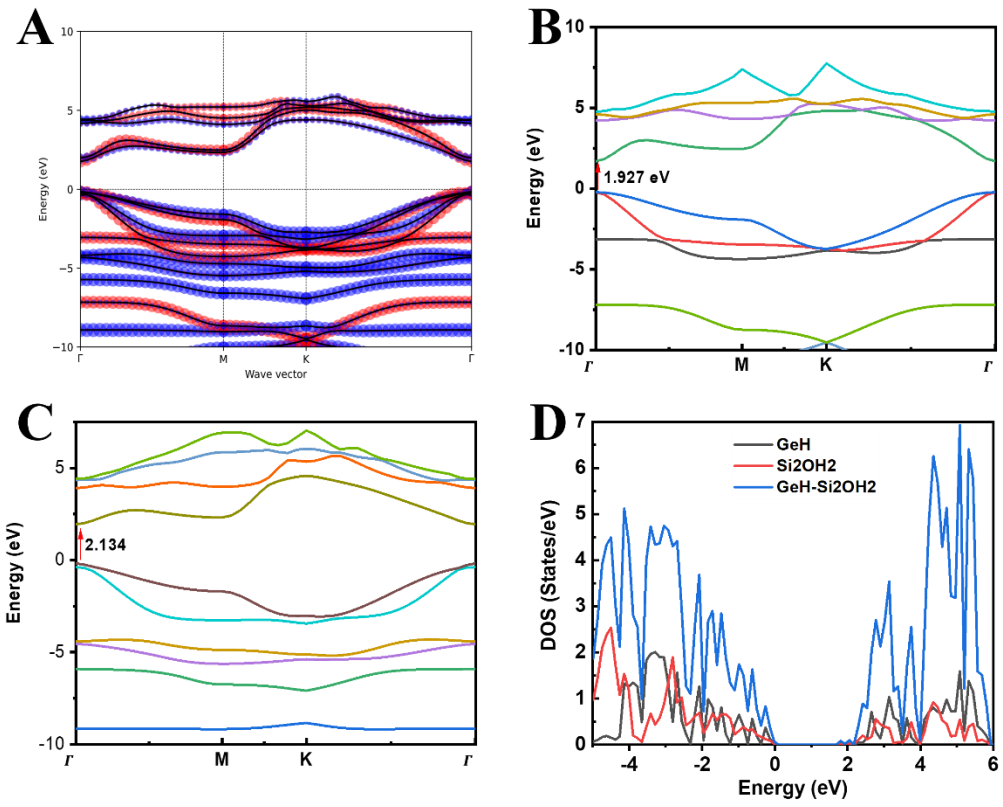

Figure S7. (A) Projected band structure of the germanane/siloxene heterostructure. (B-C) Band structures of monolayer germanane (B) and monolayer siloxene (C). (D) Total density of states of the isolated germanane and siloxene layers and the germanane/siloxene heterostructure.

To comprehensive understand the transfer mechanism of electrons in GeNSs/SiNSs heterostructure, we simulated the vdW heterostructure through constructing the germanane/siloxene heterobilayer with the thermodynamically most favorable structure in which the germanium and silicon skeletons are in AB stacking[13-15], as shown in Figure 7B, C. The electronic and optical properties of this heterobilayers was calculated. Firstly, we optimized the geometric characteristic of the germanane monolayer and siloxene monolayer. The optimized lattice parameter is 4.01 Å for germanane monolayer; whereas for siloxene monolayer, the optimized lattice parameter is 3.94 Å. Therefore, the germanane/siloxene heterobilayer was constructed with a mismatch of 1.83%. To investigate the interactions between the germanane monolayer and siloxene monolayer, the separation distance between the two layers was varied from 3.0 Å to 7.0 Å, and the stability as functions of the interlayer distances was calculated using formula (1). As shown in Figure 8A**,** the negative binding energies represent more stable structures. With the interlayer distance increase from 3.0 Å to 4.5 Å, the binding energy decreases quickly and remains positive. When the distance achieved 5.0 Å, the binding energy turns negative and maintains decreasing until the distance increase to 5.3 Å. Hence, the minimum value of the binding energy at the distance of 5.3 Å presents the most stable structure. With this most stable heterobilayer structure, we calculated the band structure and total density of states for germanane/siloxene.

As shown in Figure S7A, both the valence band maximum (VBM) and conduction band minimum (CBM) in the germanane/siloxene heterostructure are located at the ***Γ*** point, and the energy band structure of the heterostructure shows a direct band gap of 1.898 eV, which is smaller than the band gap of the germanane and siloxene monolayers (Figure S7B and C). This means that under visible light irradiation, the excitation of electrons from the VBM to the CBM in the heterostructure is easier than in the monolayer[15]. Figure S7D shows the total density of states of the heterojunction, where the electronic states of the conduction band (CB) and valence band (VB) near the Fermi energy level are hybridized by different atomic orbitals in the germanane monolayer and siloxene monolayer. The CBM is mainly composed of states from the germanane layer, while the VBM is contributed by states from the siloxene layer. Therefore, the electrons and holes in the germanane/siloxene heterojunction are distributed in the germanane and siloxene layers, respectively, which is beneficial for the separation of electrons and holes.

To investigate the optoelectronic properties of the germanane/siloxene heterostructure, we calculated the optical properties of the isolated germanane and siloxene monolayers and the heterostructure. The optical absorption coefficients $\alpha(\omega)$ were calculated by formula (2). For the siloxene monolayer and the heterostructure, since the x and y directions are symmetrically inequivalent, we calculated the absorption coefficients in these two directions separately. However, as shown in Figure 8B, C, the absorption coefficients for siloxene and the heterostructure in these two directions are only slightly different. It can be seen that both the germanane monolayer and siloxene monolayer possess high absorption coefficients from ultraviolet light to visible light with intensity of on the order of 10^5, and the absorption range of germanane monolayer is broader than that of siloxene monolayer. In particular, the light absorption intensity of

germanane monolayer could appear as large as on the order of 10^5 even in the near infrared region**.** The optical absorption coefficient curves of the germane/siloxane bilayer heterojunction in the x and y directions can almost coincide (Figure 8D), indicating that the optical absorption capacity of the bilayer heterojunction in different directions is consistent. Notably, siloxene monolayer has two optical absorption peaks with the energy of 3.08 eV and 3.75 eV, and germanane monolayer has five optical absorption peaks at 3.01, 3.45, 3.79, 4.19 and 7.53 eV, which lied in ultraviolet range, reached the intensity as large as on the order of 10^6. This indicates that they may have superior application in ultraviolet light detecting. For the germanane/siloxene heterostructure, the absorption range almost covered all the light region for germanane monolayer and siloxene monolayer, and the light absorption intensity is significantly enhanced compared with the isolated layers, especially in the ultraviolet light region. The enhanced optical absorption of the heterostructure is more suitable for photoelectronic devices. This calculation result further proves theoretically that the GeNSs/SiNSs heterojunction significantly enhances the photoelectric performance of GeNSs and SiNSs.

Table S2. Comparison of characteristic parameters of PEC type PDs

Materials	**Working wavelength**	**Test conditions**	P_{ph}**(μA cm^{-2})**	R_{ph}**(μA W^{-1})**	***D**** **（Jones）**	**Refs.**
2D BP	simulated sunlight	0.1 M KOH, 0 V	0.265	2.2	—	16
2D Bi	simulated sunlight	1.0 M NaOH, 0.5 V	0. 643	1.8	—	17
GeH	simulated light	0.5 M Na_2SO_4, 0 V	1.39	22	6.70×10^7	18
2D Te	400 nm	0.1 M KOH, 0.6 V	0.0052	2.79	6.8×10^7	19
WS_2	Simulated sunlight	0.5 M KOH, 0 V	0.2	3.75	/	20
InSe nanosheets	simulated sunlight	0.2 M KOH, 1.0 V	0.378	3.3	/	21
WS_2-TiO_2	sunlight irradiation	0.5 M Na_2SO_4, 1.0 V	0.13	0.53	/	22
SnS_2/graphene	Simulated sunlight	0 V	9×10^{-3}	9×10^{-2}	/	23
SiNSs	365 nm	0.5 M Na_2SO_4, 0.6 V	0.24	2.12	8.65×10^7	**This work**

GeNSs	520 nm	0.5 M Na_2SO_4, 0 V	0.121	1.02	2.88×10^7	**This work**
GeNSs/SiNSs-H2	520 nm	0.5 M Na_2SO_4, 0 V	0.443	3.75	1.3×10^8	**This work**

Table S3. Comparison of analytical performance of different tartrazine sensors

Sensor/Method	Linear Range	LOD	Ref.
COF/CNTs/SPCE (electrochemical)	–	7.5 nM	24
Dual-emission CQDs (ratiometric fluorescence)	0–200 μM	0.10 μM	25
ZnO/MWCNT/GCE (voltammetric)	10–100 μM	2.21 nM	26
B-O-CDs (ratiometric fluorescence)	0.2–60 μM	64 nM	27
Polyglycine/CPE (CV)	1–27 and 35–87 μM	0.283 μM	28
Poly (p-aminobenzenesulfonic acid)/ZnO nanoparticles-CPE (DPV)	0.0349–1.246 and 1.246–5.44 μM	0.080 μM	29
Electropolymerized hemin/GCE (SWV)	0.5-10 μM	0.360 μM	30
Poly(L-methionine)/Reduced graphene oxide/SPCE (DPV)	1–10 and 10–85μM	0.041 μM	31
Poly(L-cysteine)/Ag nanoparticles/GCE (DPV)	0.75–75 and 75–750 μM	0.25 μM	32
MoS_2/GCE (photoelectrochemical)	2.9–144 μM	41 nM	33
GeNSs/SiNSs PEC sensor	**1 pM – 1 μM**	**0.3 pM**	**This work**

Nomenclature: Covalent Organic Frameworks (COF); Carbon Nanotubes (CNTs); Carbon Quantum Dots (CQDs); Multi-walled Carbon Nanotube (MWCNT); Blue- and orange-emissive carbon dots (B-O-CDs); Screen printed carbon electrode (SPCE); Carbon paste electrode **(**CPE**);** Cyclic voltammetry (CV); Differential pulse voltammetry (DPV); Glassy carbon electrode (GCE); Square-wave voltammetry (SWV).

References

1. Bianco E, Butler S, Jiang S, *et al.* Stability and exfoliation of germanane: A germanium graphane analogue. *ACS Nano.* **2013**; *7* (5): 4414–4421. https://doi.org/10.1021/nn4009406
2. Zhao F, Feng Y, Wang Y, *et al*. Two-dimensional gersiloxenes with tunable bandgap for photocatalytic H_2 evolution and CO_2 photoreduction to CO.

Nat. Commun. **2020**; *11* (1): 1-13. https://doi.org/10.1038/s41467-020-15262-4

3. Kresse G, Furthmüller J. Efficiency of ab-initio total energy calculations fo r metals and semiconductors using a plane-wave basis set. *Comput. Mater. Sci.* **1996**; *6* (1): 15-50. https://doi.org/10.1016/0927-0256(96)00008-0
4. Kresse G, Furthmüller J. Efficient iterative schemes for ab initio total-ener gy calculations using a plane-wave basis set. *Phys. Rev. B* **1996**; *54* (16): 11169-11186. https://doi.org/10.1103/PhysRevB.54.11169
5. Perdew J P, Burke K, Ernzerhof M. Generalized Gradient Approximation Made Simple. *Phys. Rev. Lett.* **1996**; *77* (18): 3865-3868. https://doi.org/10. 1103/PhysRevLett.77.3865
6. Grimme S. Semiempirical GGA-type density functional constructed with a l ong-range dispersion correction. *J. Comput. Chem.* **2006**; *27* (15): 1787-179 9. https://doi.org/10.1002/jcc.20495
7. Kresse G, Joubert D. From ultrasoft pseudopotentials to the projector augm ented-wave method. *Phys. Rev. B.* **1999**; *59* (3): 1758-1775. https://doi.org/1 0.1103/PhysRevB.59.1758
8. Blöchl P E. Projector augmented-wave method. *Phys. Rev. B.* **1994**; *50* (2 4): 17953-17979. https://doi.org/10.1103/PhysRevB.50.17953
9. Methfessel M, Paxton A. T. High-precision sampling for Brillouin-zone inte gration in metals. *Phys. Rev. B.* **1989**; *40* (6): 3616-3621. https://doi.org/10. 1103/PhysRevB.40.3616
10. Blöchl P E, Jepsen O, Andersen O K. Improved tetrahedron method for B rillouin-zone integrations. *Phys. Rev. B.* **1994**; *49* (23): 16223-16233. https:/ /doi.org/10.1103/PhysRevB.49.16223
11. Guo Q, Han Y, Chen N, *et al.* Few-Layer Siloxene as an Electrode for Su perior High-Rate Zinc Ion Hybrid Capacitors. *ACS Energy Lett.* **2021**; *6* (5): 1786-1794. https://doi.org/10.1021/acsenergylett.1c00285
12. Krishnamoorthy K, Pazhamalai P, Kim S-J. Two-dimensional siloxene nano sheets: novel high-performance supercapacitor electrode materials. *Energy E nviron. Sci.* **2018**; *11* (6): 1595-1602. https://doi.org/10.1039/C8EE00160J
13. Li Y, Chen Z. XH/pi (X = C, Si) Interactions in Graphene and Silicene: Weak in Strength, Strong in Tuning Band Structures. *J. Phys. Chem. Lett.* **2013**; *4* (2): 269-275. https://doi.org/10.1021/jz301821n
14. Jin H, Dai Y, Ma X.-C, *et al.* Enhancement of photocatalytic activity of a two-dimensional GeH/graphene heterobilayer under visible light. *RSC Adv.* **2015**; *5* (64): 52264-52268. https://doi.org/10.1039/c5ra07549a
15. Shang J, Pan L, Wang X, *et al.* Tunable electronic and optical properties of InSe/InTe van der Waals heterostructures toward optoelectronic applicatio ns. *J. Mater. Chem. C* **2018**; *6* (27): 7201-7206. https://doi.org/10.1039/C8T C01533C
16. Ren X, Li Z, Huang Z, *et al.* Environmentally Robust Black Phosphorus Nanosheets in Solution: Application for Self-Powered Photodetector. *Adv F unct Mater*. 2017; 27(18): 1606834. https://doi.org/10.1002/adfm.201606834

17. Huang H, Ren X, Li Z, *et al.* Two-dimensional bismuth nanosheets as pro spective photo-detector with tunable optoelectronic performance. *Nanotechno logy*. 2018; 29(23): 235201. https://doi.org/10.1088/1361-6528/aab6ee
18. Liu N, Qiao H, Xu K, *et al.* Hydrogen terminated germanene for a robust self-powered flexible photoelectrochemical photodetector. *Small*. 2020; 16(2 3): 2000283. https://doi.org/10.1002/smll.202000283
19. Xie Z, Xing C, Huang W, *et al.* Ultrathin 2D Nonlayered Tellurium Nanos heets: Facile Liquid-Phase Exfoliation, Characterization, and Photoresponse with High Performance and Enhanced Stability. *Adv Funct Mater*. 2018; 28 (16): 1705833. https://doi.org/10.1002/adfm.201705833
20. Wang B, Zhu W, Tang P, *et al.* Graphene–like tungsten sulphide nanosheet s prepared by hydrothermal intercalation/exfoliation route and its applicatio n for photodetector. *Fullerenes, Nanotubes Carbon Nanostruct*. 2019; 27(1 2): 928-933. https://doi.org/10.1080/1536383X.2019.1663343
21. Li Z, Qiao H, Guo Z, *et al.* High-Performance Photo-Electrochemical Phot odetector Based on Liquid-Exfoliated Few-Layered InSe Nanosheets with E nhanced Stability. *Adv Funct Mater*. 2018; 28(16): 1705237. https://doi.org/ 10.1002/adfm.201705237
22. Ren X, Qiao H, Huang Z, *et al.* Investigating the photocurrent generation and optoelectronic responsivity of WS_2-TiO_2 heterostructure. *Opt Commun*. 2018; 406: 118-123. https://doi.org/10.1016/j.optcom.2017.07.033
23. Qiao H, Chen X, Wang B, *et al.* Novel tin disulfide/graphene photoelectro chemical photodetector based on solid-state electrolytes and its performance s. *J Mater Sci: Mater Electron*. 2019; 30(4): 3208-3213. https://doi.org/10.1 007/s10854-019-00689-3
24. Yeh C-L, Ceng Y-J, Huang M-X, *et al.* Triazine-based COF/CNTs as an el ectrochemical sensor for the simultaneous detection of sunset yellow and ta rtrazine in food samples. *Anal. Methods* 2025; 17 (26): 5392–5399. https:// doi.org/10.1039/d5ay00708a
25. Chen Z, Peng Y, Liu S, *et al.* Synthesis of dual-emission carbon quantum dots for ratiometric fluorescence detection of tartrazine. *Dyes Pigm.* 2026; 245: 113189. https://doi.org/10.1016/j.dyepig.2025.113189
26. Suma J G, Kotabagi S D, Megalamani M B, *et al.* A rapid and sensitive method for the determination of Tartrazine using ZnO/MWCNT modified el ectrode. *Sustain. Chem. One World* 2026; 11: 100261. https://doi.org/10.101 6/j.scowo.2026.100261
27. Safaei A, Giyahban F, Ebrahimzadeh H, *et al.* Development of a ratiometri c fluorescence sensor based on blue- and orange-emissive carbon dots for t he determination of tartrazine in food products. *Food Chem.* 2025; 477: 14 3582. https://doi.org/10.1016/j.foodchem.2025.143582
28. Manjunatha J G. A novel voltammetric method for the enhanced detection of the food additive tartrazine using an electrochemical sensor. *Heliyon* 201 8; 4: e00986. https://doi.org/10.1016/j.heliyon.2018.e00986
29. Karim-Nezhad G, Khorablou Z, Zamani M, *et al.* Voltammetric sensor for

tartrazine determination in soft drinks using poly (p-aminobenzenesulfonic a cid)/zinc oxide nanoparticles in carbon paste electrode. *J. Food Drug Anal.* 2017; 25: 293–301. https://doi.org/10.1016/j.jfda.2016.10.002

30. Sun S-C, Hsieh B-C, Chuang M-C. Electropolymerised-hemin-catalysed red uction and analysis of tartrazine and sunset yellow. *Electrochim. Acta* 2019; 319: 766–774. https://doi.org/10.1016/j.electacta.2019.07.014
31. Akkapinyo C, Subannajui K, Poo-arporn Y, *et al.* Disposable Electrochemic al Sensor for Food Colorants Detection by Reduced Graphene Oxide and Methionine Film Modified Screen Printed Carbon Electrode. *Molecules* 202 1; 26: 2312. https://doi.org/10.3390/molecules26082312
32. Tang Y, Wang Y, Liu G, *et al.* Determination of sunset yellow and tartrazi ne using silver and poly (L-cysteine) composite film modified glassy carbo n electrode. *Indian J. Chem.* 2016; 55A: 298–303. https://api.semanticschola r.org/CorpusID:52218752
33. Chen Z, Arumugam D, Kesavan J, *et al.* Advanced MoS_2-Based Electroche mical Platform for Trace Tartrazine Detection With Light-Enhanced Signal Amplification. *ChemistrySelect* 2026; 11 (13): e04906. https://doi.org/10.100 2/slct.202504906